

ORIGINAL ARTICLE

Geometric calibration of a computed laminography system for high-magnification nondestructive test imaging

Seung-Hoon Chae  | Kihong Son  | Sooyeul Lee 

Medical Information Research Section,
Electronics and Telecommunications
Research Institute, Daejeon, Republic of
Korea

Correspondence

Sooyeul Lee, Medical Information
Research Section, Electronics and
Telecommunications Research Institute,
Daejeon, Republic of Korea.
Email: seq@etri.re.kr

Funding information

This work was supported by the Korea
Medical Device Development Fund grant
funded by the Korea government (the
Ministry of Science and ICT, the Ministry
of Trade, Industry and Energy, the
Ministry of Health & Welfare, the
Ministry of Food and Drug Safety)
(Project Number:
KMDF_PR_20200901_0016,
9 991 006 689).

Abstract

Nondestructive testing, which can monitor a product's interior without disassembly, is becoming increasingly essential for industrial inspection. Computed laminography (CL) is widely used in this application, as it can reconstruct a product, such as a printed circuit board, into a three-dimensional (3D) high-magnification image using X-rays. However, such high-magnification scanning environments can be affected by minute vibrations of the CL device, which can generate motion artifacts in the 3D reconstructed image. Since such vibrations are irregular, geometric corrections must be performed at every scan. In this paper, we propose a geometry calibration method that can correct the geometric information of CL scans based on the image without using geometry calibration phantoms. The proposed method compares the projection and digitally reconstructed radiography images to measure the geometric error. To validate the proposed method, we used both numerical phantom images at various magnifications and images obtained from real industrial CL equipment. The experiment results confirmed that sharpness and contrast-to-noise ratio (CNR) were improved.

KEYWORDS

computed laminography, geometry calibration, high-magnification, motion artifacts, mutual information, nondestructive testing

1 | INTRODUCTION

1.1 | Nondestructive testing and computed laminography

Nondestructive testing (NDT) is critical in the quality testing of various industrial devices [1]. The importance of NDT increases as products, such as integrated circuit (IC) packaging, become smaller and the complexity of

their structure increases [2]. In particular, using X-ray computed tomography (CT) is becoming increasingly popular, as it can reconstruct and analyze three-dimensional images (3D) [1–7]. CT operates using the attenuation coefficient of X-rays transmitted through a material to form a 3D image. It effectively inspects a structure's interior by filtering the projection images acquired from various directions around the rotation axis and projecting them back [6,8–10]. However, CT

Seung-Hoon Chae and Kihong Son contributed equally to this work.

This is an Open Access article distributed under the term of Korea Open Government License (KOGL) Type 4: Source Indication + Commercial Use Prohibition + Change Prohibition (<http://www.kogl.or.kr/info/licenseTypeEn.do>).

1225-6463/\$ © 2022 ETRI

equipment has limitations in imaging samples with plate-like structures, such as ICs and multilayer printed circuit boards (PCBs) [1–3,6,7]. First, obtaining projection images by rotating a platelike sample does not provide sufficient projection information in a specific angular range according to the shape and thickness of the sample [3,5]. Additionally, even if the projection images were acquired using high-energy X-rays with enough flux, differences in the X-ray transmission path length and its effects by scattering, beam hardening, and photon starvation, and so on, would significantly degrade the quality and spatial resolution of the reconstructed images. Second, a sufficient distance between the source and sample is required to avoid collisions, reducing the magnification and spatial resolution of the CT images [5,6]. One approach to overcoming the above limitations is rotational computed laminography (CL) [1–5], which is based on the relative motion of the X-ray source, detector, and sample. By tilting the X-ray beam line relative to the rotation axis of a flat sample at an arbitrary angle, the X-ray beam passes through a similar thickness over the flat sample. The main difference between CL and CT is the tilted rotation axis [1]. Using rotational CL, magnification can be controlled by adjusting the distance between the source and the object and changing the scan field of view (FOV) according to the degree of the tilted angle [5,6]. Therefore, improving the spatial resolution and quality of the reconstructed images is possible using rotational CL, increasing its usefulness and effectiveness in NDT [1,2,6,9,11].

To reconstruct projection images into a 3D image, geometric information on X-ray CT scanners, such as source and detector positions, that is, (S_x, S_y, S_z) and (D_x, D_y, D_z) (Figure 1), source-to-object distance (SOD), source-to-detector distance (SDD), and object-to-detector distance (ODD), is required. This geometric information is determined before X-ray scanning. However, when acquiring a projection image, distortions, or

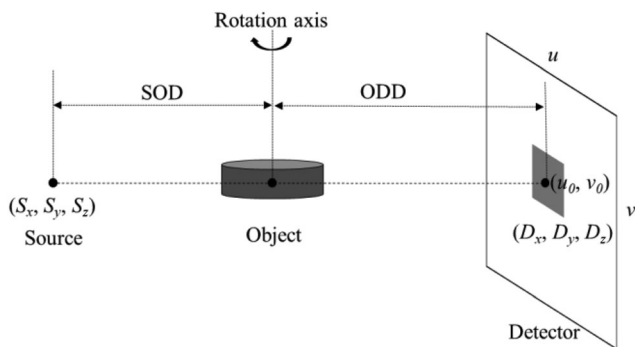


FIGURE 1 Geometry information of X-ray computed tomography (CT) scanner

vibrations of the scanning device can introduce errors to the geometric information, such as the center of rotation (COR), tilting angle, and SDD. Figure 2 shows errors caused by geometric misinformation. When the object or detector wobbles, certain projection images can be back-projected to a misaligned location (Figure 2B,C). This is because back-projection is performed according to the predetermined geometric information. This may obscure minute defects inside samples or deteriorate the image quality during quality inspection [1,6–9]. Several methods have been proposed to correct this geometrical error, but most have limitations requiring a scanned image for a dedicated phantom. In methods that do not use a dedicated phantom, only the global COR is corrected among various causes of geometric errors.

In addition, existing studies have been conducted on only low magnifications of $2\times$ or below [6–9,12,13]. Recently, the implementation of high-magnification scans, which can minimize the distance between the

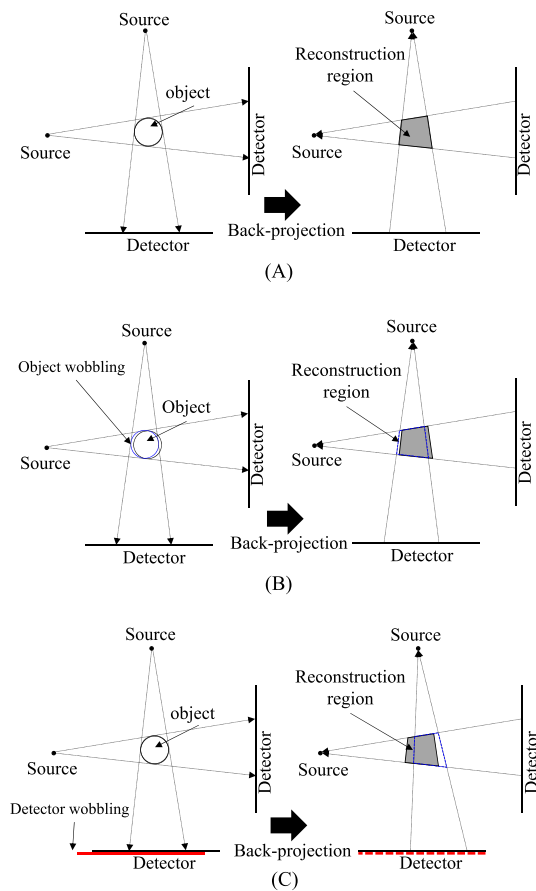


FIGURE 2 Examples of errors caused by geometry misinformation: (A) the exact scan case, (B) the example of an object wobbling, and (C) the example of a detector wobbling (red line: detector wobbling error when scanning; red dot: the predetermined location of the detector)

source and sample, has become more popular and allowed for more precise inspections. However, as this method is sensitive to scanning device distortions or vibrations, an effective reconstruction method that corrects geometric errors and minimizes the deterioration of image quality is necessary.

1.2 | Geometric calibration phantom-based calibration method

Geometric calibration phantom (GCP)-based calibration methods can be used to correct the geometric motion of cone beam CT equipment. The GCP-based calibration method converts the two-dimensional (2D)–3D mapping relationship between each voxel of the reconstructed volume and the pixel of the projected image into a 3×4 matrix, called the projection matrix (PM). By scanning a predesigned geometry calibration phantom, the geometric information of each projection is determined by utilizing the correspondence between each feature point in the phantom and the projected image for each angle. The matrix can be calculated by imaging the dedicated phantom, composed of multiple metal beads, and establishing the correspondence between the 3D positions of the metal beads and the projected 2D bead positions in the radiographic projection image [14–17]. The PM is expressed as (1). Here, $[R|Tr]$ is 3×4 matrix representing the rotation and translation of the source coordinate relative to the object or reconstruction coordinate, respectively. (u_0, v_0) is a detector offset (in pixels) where X-ray beams are incident vertically on the detector.

$$\begin{bmatrix} u \\ v \\ 1 \end{bmatrix} \propto \text{PM} \begin{bmatrix} x \\ y \\ z \\ 1 \end{bmatrix} = \begin{bmatrix} \frac{\text{SDD}}{u_{\text{pitch}}} & -u_0 & 0 \\ 0 & -v_0 & \frac{\text{SDD}}{v_{\text{pitch}}} \\ 0 & -1 & 0 \end{bmatrix} [R|Tr] \begin{bmatrix} x \\ y \\ z \\ 1 \end{bmatrix}. \quad (1)$$

However, there are some limitations in applying the GCP-based calibration method to a high-magnification CL scan. First, prior GCP-based calibration information cannot be made for all possible cases, such as the set position of the COR of the sample, tilting angle of the detector, distance between the source and the detector, and repeatability of the scanning device movement must be guaranteed. Second, a special small-scale GCP is required for image correction at high magnification, and obtaining an image by precisely set-positioning the phantom and sample alternately at the same location in the CL device for actual use is difficult. Therefore, we propose a geometric correction method that does not require a GCP or

its scan. The correction method was developed to minimize geometric errors by comparing the projected image of each sample angle and the digitally reconstructed radiography (DRR) image generated from the reconstructed 3D image. Compared to the existing COR method, which finds and corrects only a single global rotational center position, the proposed method performs correction more accurately by reflecting the motion caused by the translation and rotation of the scanning device for each projection.

2 | MATERIALS AND METHODS

2.1 | Study design

The geometric calibration method (GCM) for the high-magnification CL system proposed in this paper reconstructed an image using an updated PM, which was obtained based on a geometric correction value calculated using mutual information (MI) between the projected and DRR images. We calculated the geometric correction performance using a numerical phantom for simulations and images acquired from an industrial CL device to evaluate the proposed method. The numerical phantom for the simulations took the form of a plate-shaped substrate in which cylindrical markers were arranged in 2D. The data acquired from the actual CL device were images of PCBs.

2.2 | Projection and digitally reconstructed radiography image-based geometric calibration method

This paper proposes a projection and DRR image-based GCM (PDGCM). PDGCM is a method of generating an updated PM that corrects the geometric information of the scanning device by comparing the reconstructed CL image and projection images (P) using the initial PM generated based on the prior known geometric information of the scanning device. Figure 3 shows the entire process of the proposed PDGCM.

To compare the P and CL images, the CL volume is forward-projected at the same angle as the P scan angle, which is used to acquire DRR images (D). In the image registration step, $P(i)$ and $D(i)$ are compared to find the optimally matched transformation information $T(i)$, that is, translation and rotation. Here, i refers to the index of the projection images. In the image registration step, various registration algorithms may be used. In this paper, MI, commonly used for X-ray image matching, was applied [10,18]. We used the gradient descent method for

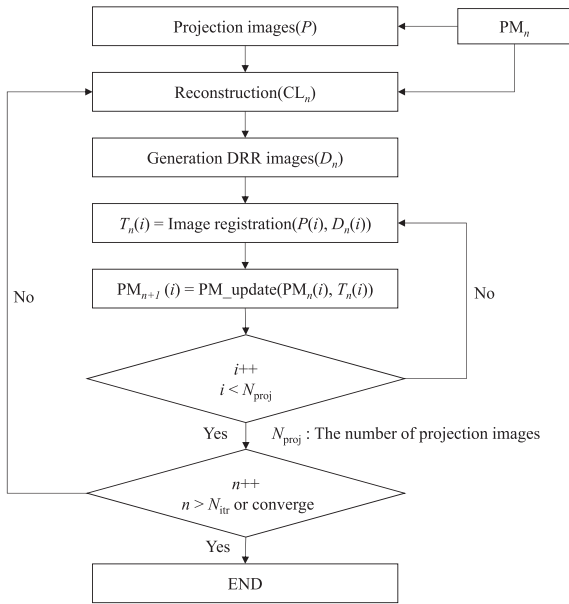


FIGURE 3 Flow chart illustrating the projection and digitally reconstructed radiography image-based geometric calibration method (PDGCM)

MI optimization. After calculating the corrected PM by reflecting the calculated translation and rotation information against the initial PM, CL image reconstruction is performed with the corrected PM. After the above process is repeated several times, either a particular number of times (N_{itr}) or until the values converge, a geometrically corrected CL image is obtained.

2.3 | Simulation study

To quantitatively and systemically evaluate our PDGCM's performance, we simulated a platelike sample and used several numerical phantoms of various magnifications. To simulate a shape similar to a PCB and ball grid array (BGA) of an electronic device, a thin plate-shaped space was created, and cylindrical markers were arranged at regular intervals (Figure 4).

By adjusting the SOD between the source and the plate-shaped phantom, forward-projection images of the numerical phantom were generated at 10 \times , 25 \times , 50 \times , and 100 \times magnifications. After generating the initial PM according to the scan conditions shown in Table 1, the image was reconstructed to generate ground truth (GT) volume data.

In addition, the plate-shaped phantom for each angle was shifted by 0.05 mm in the horizontal (u) direction of the detector to accommodate the magnitude of vibration of the industrial CL device. This allowed a simulation to be performed so that the motion artifacts of the scanning

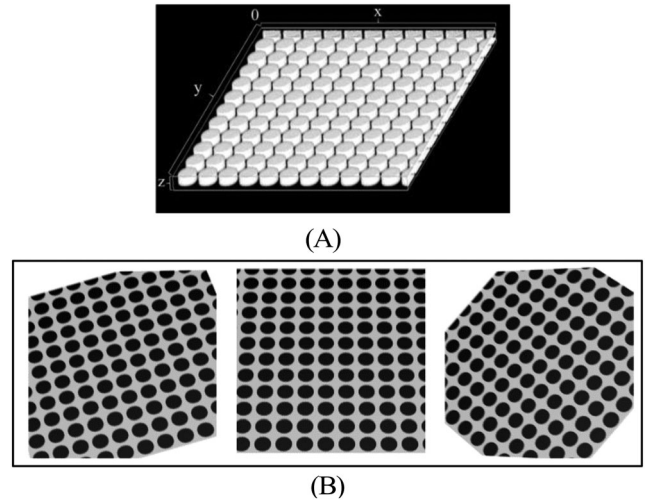


FIGURE 4 (A) Volume of numerical phantoms and (B) forward projection images from the numerical phantoms

TABLE 1 Specifications of the numerical phantom used in the simulation study

Parameter	Value
The numerical phantom volume (pixel)	$576 \times 576 \times 20$
Detector array size (pixel)	1152×1152
Detector pitch (mm)	0.099×0.099
Object-to-detector distance (mm)	500.0
Tilting angle ($^{\circ}$)	60.0
Magnification	10, 25, 50, 100
Angular interval ($^{\circ}$)	1

device appeared in the reconstructed image. The ODD was fixed at 500 mm, and the SOD was changed to create numerical phantoms between 10 \times and 100 \times magnifications.

2.4 | Experimental study

Figure 5 is a schematic of the industrial rotary laminography system we used. The plate-shaped sample placed on the stage could rotate around the axis of rotation, and the axis of rotation passed through a point in the sample perpendicular to the stage. The stage could move up, down, and horizontally to any position, allowing arbitrary magnification and FOV adjustments. The closer the sample was to the X-ray source, the higher the image magnification, where magnification refers to the ratio of the SDD to SOD. During CL scanning, the tilt angle of the detector

was set at a specific value along the C-arm rail (maximum $\alpha = 70^\circ$), the plate-shaped sample was rotated 360° on the stage, and CL images were obtained at 1° angular intervals.

We verified the performance of the proposed algorithm using plate-shaped sample images acquired from industrial CL scan equipment. For our experiments, we obtained data for four different samples, whose magnifications are listed in Table 2.

When evaluating the actual scan experiment image, the global sharpness (S_{global}), boundary sharpness (S_{boundary}), and contrast-to-noise ratio (CNR) were measured for quantitative evaluation [11]. To calculate the sharpness of the volume image, volume data were calculated for each slice [19].

The S_{global} value is defined as follows:

$$S_{\text{global}} = \sum_{x=1}^M \sum_{y=1}^N \sqrt{\left(\frac{\partial I}{\partial x}\right)^2 + \left(\frac{\partial I}{\partial y}\right)^2}, \quad (2)$$

where I denotes the image of $M \times N$ size.

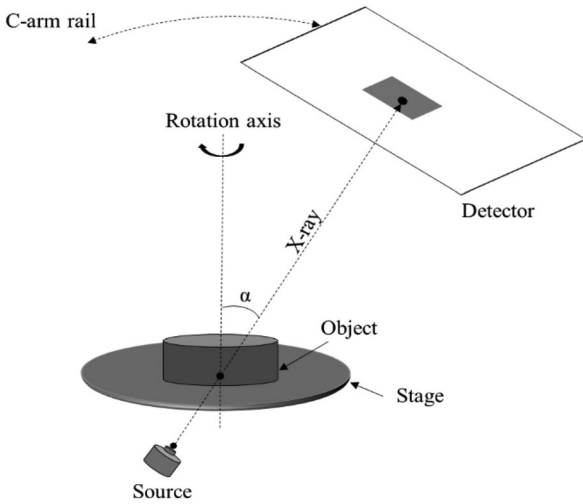


FIGURE 5 Schematic of an industrial computed laminography (CL) scan system

TABLE 2 Magnification information for each sample case

Data	SOD (mm)	ODD (mm)	Magnification	Tilting angle ($^\circ$)
Case 1	39.20	498.14	13.70	60
Case 2	18.40	495.75	27.94	60
Case 3	13.00	499.02	39.38	60
Case 4	5.42	495.75	92.46	60

Abbreviations: ODD, object-to-detector distance; SOD, source-to-object distance.

The S_{boundary} is a method of measuring the sharpness of an object's boundary. The S_{boundary} value is defined as follows:

$$S_{\text{boundary}} = \sum_{(x,y) \in R_{\text{margin}}} \sqrt{\left(\frac{\partial I}{\partial x}\right)^2 + \left(\frac{\partial I}{\partial y}\right)^2}, \quad (3)$$

where R_{margin} denotes the object boundary.

The following equation was used to evaluate the CNR of the image:

$$\text{CNR} = \frac{\overline{I_{\text{ROI}}} - \overline{I_{\text{BG}}}}{\sigma_{\text{BG}}}. \quad (4)$$

$\overline{I_{\text{ROI}}}$ means the average brightness of the selected region of interest (ROI), and I_{BG} means the average brightness of the background. The background was set as the area around the selected ROI. To select the ROI, the threshold method was used.

3 | RESULTS

3.1 | Simulation study results

Figure 6 shows three reconstruction images (GT, before PDGCM, and after PDGCM) and the results before and after correction according to the magnification at the center slice of the reconstruction volume. These images confirmed that the motion artifacts reduced after geometric correction at all magnifications, resulting in a shape and brightness similar to that of the GT. In particular, the edge of the cylindrical shape, which was blurred before correction, became sharper after correction, and the contrast was improved.

Table 3 shows the results of the structural similarity (SSIM) [20] and normalized root-mean-square error (NRMSE) according to the magnification. To compare the results based on magnification only, the same ROI in the image was used, as shown in the red box in Figure 6. To make the FOV size of the comparison area the same in each magnification image, the ROI size was set according to the FOV size of the $100\times$ magnification image.

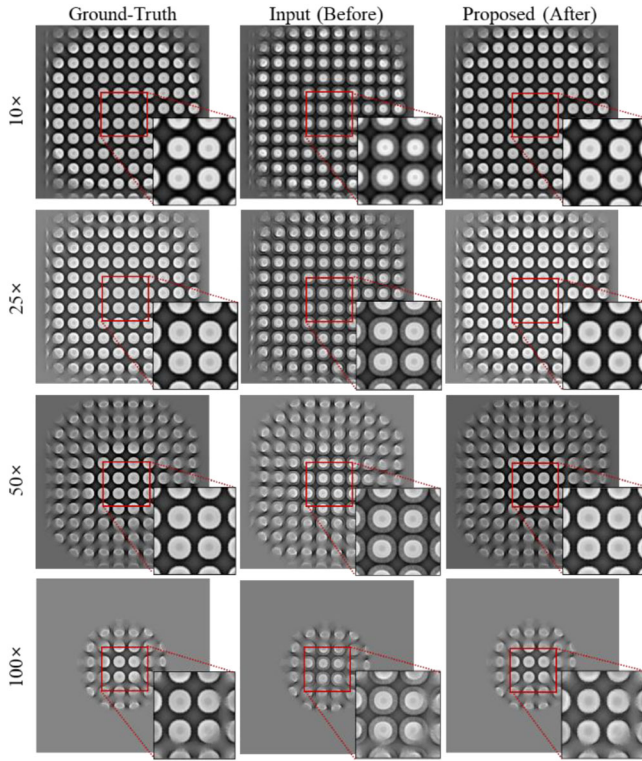


FIGURE 6 Reconstruction images (ground truth [GT], before projection and digitally reconstructed radiography image-based geometric calibration method [PDGCM], and after PDGCM), showing reduced artifacts at all magnifications

TABLE 3 SSIM and NRMSE results of the simulation image. NRMSE increased with increasing magnification; conversely, the SSIM value decreased with increasing magnification.

Data		SSIM	NRMSE
10×	Before	0.2321	20.54
	After	0.9962	1.27
25×	Before	0.1937	23.59
	After	0.9730	3.64
50×	Before	0.1796	23.36
	After	0.9693	7.26
100×	Before	0.3060	19.40
	After	0.8770	5.64

Abbreviations: NRMSE, normalized root-mean-square error; SSIM, structural similarity.

TABLE 4 MSE results for the simulation image

Method	10 mag.	25 mag.	50 mag.	100 mag.
MSE	0.01 mm ± 0.002	0.0086 mm ± 0.00085	0.0055 mm ± 0.00116	0.0116 mm ± 0.01174

MSE, mean squared error.

The NRMSE of the ROI is given by the following equation:

$$\text{NRMSE} = \frac{\text{RMSE}}{x_{\max} - x_{\min}} \quad \text{and} \quad (5)$$

$$\text{RMSE} = \sqrt{\frac{1}{N} \sum_{i=1}^N \{x(i) - x'(i)\}^2} \quad (6)$$

N : The number of pixels

where x and x' denote the ROI of GT and the ROI of the image for evaluation and x_{\max} and x_{\min} represent the maximum and minimum values of the ROI of GT, respectively. The evaluation results confirmed that the SSIM and NRMSE were significantly improved compared to before the correction for all magnifications. In particular, the SSIM value was 0.96 or above for the 10×, 25×, and 50× magnifications; however, at 100×, it was around 0.877, which shows a decrease in performance by about 10% compared to the magnification at 50×. We believe that the larger magnification led to insufficient image information for the PDGCM correction, resulting in decreased accuracy. The root-mean-square error (RMSE) value also decreased after calibration compared to before calibration; as the magnification decreased, the RMSE value decreased. The computational simulation phantom created motion-induced artifacts in the reconstructed CL volume image by artificially changing the PM with introduced errors to u_{offset} and v_{offset} . Therefore, the correction error was calculated by comparing the previously known u_{offset} and v_{offset} information of the GT with the u'_{offset} and v'_{offset} information for each projection corrected through the PDGCM. The mean squared error (MSE) was used to calculate the correction error (7), and Table 4 shows the results.

$$\text{MSE} = \frac{1}{N_{\text{proj}}} \sum_{i=1}^{N_{\text{proj}}} \{ (u(i)_{\text{offset}} - u'(i)_{\text{offset}})^2 + (v(i)_{\text{offset}} - v'(i)_{\text{offset}})^2 \}. \quad (7)$$

The results of the simulation study were confirmed to have an error below 0.01 mm on average, which is 1 voxel error based on a computational phantom with a voxel

pitch of 0.01 mm. The performance was greatly improved at 10 \times , 25 \times , and 50 \times magnifications, but at 100 \times , the performance decreased slightly.

3.2 | Experimental study results

Our experimental study compared the simulated results with geometric corrections of an actual scan image of the BGA of a PCB. The performance results were compared for four cases at different magnifications. Figure 7 shows the results of the PDGCM, which clearly shows that the image quality was improved as the edge of the BGA in the corrected image is clearer than before.

Figure 8 shows the axial, sagittal, and coronal planes of the red dot area for each case in Figure 7, which shows that the artifacts were reduced after geometric correction.

For quantitative evaluations of the proposed method, reconstructed images after corrections are analyzed in terms of S_{global} , S_{boundary} , and CNR. The average value of global sharpness S_{global} was calculated in ± 5 slices centered on the central slice. As the S_{global} value increases, the object's detail, such as the edge of the bead, is better reconstructed than that before the correction.

The S_{boundary} was calculated only in the margin area. The margin setting was done using the threshold method and morphology operation. After creating a segmentation mask using the Otsu method, the margin mask (Figure 9) was created by performing the difference calculation between the mask to which the dilation was applied and the mask to which the erosion was applied.

For the CNR calculation, the ROI mask is selected on the BGA area using the threshold method, and the

background mask is set around the selected ROI (Figure 10). A margin was given between the ROI and background area so they did not overlap. Table 5 shows the calculated values of S_{global} , S_{boundary} , and CNR. The calculation results show that the S_{global} , S_{boundary} , and CNR values are improved after applying our method in all cases. In addition, the improvement rate of our method showed higher results than the COR method. In particular, the CNR value improved by 34% on average. Similar to the simulation results, the effects of the correction were relatively large at low magnifications, and the degree of correction tended to decrease at high magnifications.

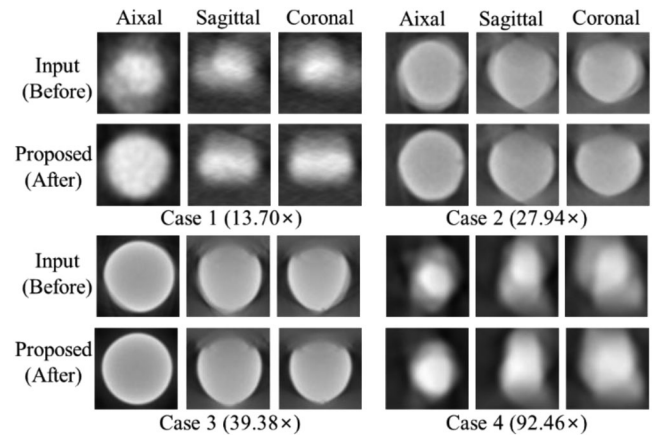


FIGURE 8 Axial, sagittal, and coronal image results of computed laminography (CL) volume, which show that the shape of the bead changed due to the geometry calibration

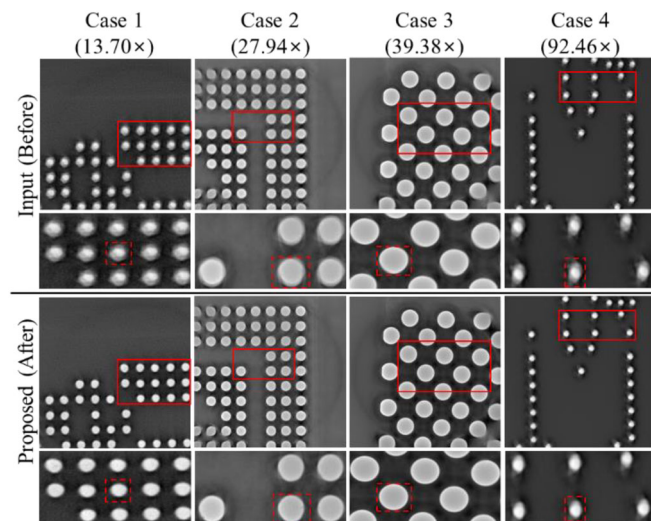


FIGURE 7 Images before and after the geometry calibration of the actual scan images

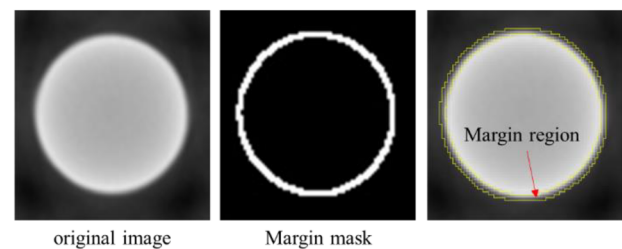


FIGURE 9 Process of setting the margin in the region of interest (ROI) part of the scan object

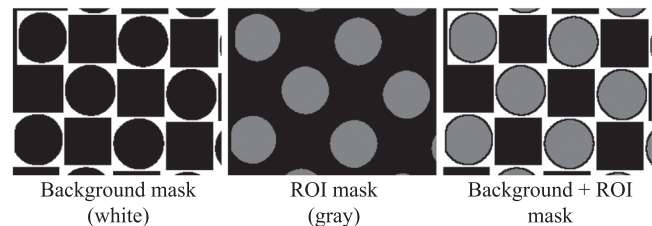


FIGURE 10 Area used for contrast-to-noise ratio (CNR) calculation: White is background and gray is region of interest (ROI)

TABLE 5 Sharpness and CNR results for the experimental images

Data		S_{global}	S_{boundary}	CNR
Case 1 (13.70 \times)	Input	118.63 \pm 39.78	3160.37 \pm 344.08	6.13 \pm 0.38
	COR	1205.81 \pm 40.79	3651.70 \pm 453.89	5.71 \pm 0.29
	Our method	1246.56 \pm 28.34	3752.29 \pm 461.61	9.64 \pm 0.81
Case 2 (27.94 \times)	Input	671.21 \pm 11.36	1808.12 \pm 401.04	6.16 \pm 1.17
	COR	693.83 \pm 14.71	1891.43 \pm 480.14	7.42 \pm 1.57
	Our method	694.58 \pm 12.10	2238.93 \pm 528.61	7.84 \pm 1.81
Case 3 (39.38 \times)	Input	1010.02 \pm 10.12	2255.68 \pm 604.48	8.71 \pm 1.87
	COR	1066.01 \pm 11.629	2362.85 \pm 648.21	9.46 \pm 2.09
	Our method	1062.55 \pm 12.95	2518.97 \pm 775.52	11.45 \pm 2.83
Case 4 (92.46 \times)	Input	289.45 \pm 2.78	2129.62 \pm 230.16	4.69 \pm 0.40
	COR	285.23 \pm 2.48	2412.23 \pm 277.84	5.07 \pm 0.26
	Our method	296.19 \pm 4.01	2349.64 \pm 305.60	5.65 \pm 0.43

Note: Boldface data show the best performance.

CNR, contrast-to-noise ratio.

4 | DISCUSSION

NDT using rotational CL produces high-resolution and -magnification images by reducing the distance between the source and the object. However, these images are sensitive to the operational vibrations of the scanning device, which can result in motion-induced artifacts, such as blurring or distortion. In this study, we developed a PDGCM to correct motion-induced artifacts in high-magnification CL reconstructed images. Various studies have demonstrated methods to compensate for such artifacts, but they require dedicated phantoms, which are only valid for low magnifications (i.e., $<2\times$) [13,21,22]. Our PDGCM functions up to $100\times$ magnification and performs automatic geometry corrections based on the PDGCM, using acquired sample images without dedicated phantoms. The numerical phantom simulations demonstrated that the error was within an average of 0.012 mm for all magnifications after correction. Next, the performance of the algorithm was evaluated using the actual scan image reflecting the physical properties and shape, among others, of the object to be inspected. The PDGCM improved the sharpness and CNR of real PCB images by approximately 16% and 33%, respectively. Furthermore, the images resulting from geometric correction also showed improved contrast, clear edge distinction, and reduced noise and blurring. Our simulation and experimental studies showed significant improvements in image quality and artifact reduction. However, the accuracy was reduced at a relatively high magnification of $100\times$. This is possibly because higher

magnification increases sensitivity to small movements and because the amount of information used for the PDGCM calculations decreases due to small reconstruction FOV. Furthermore, in the case of multilayer PCBs with complex structures, although not covered in this work, there will possibly be restrictions on accurate geometric correction due to complex low-contrast overlapping information from each layer in the projection image. Therefore, it is considered that additional studies, such as applying various iterative reconstruction methods or deep learning [23,24] to improve accuracy in ultra-high magnification and multilayer geometry correction, are necessary for the future. We believe that our method can be useful not only in the industrial field but also in the medical field. In industrial sites, cone beam CT imaging systems are used frequently. Our study can also be applied to electrode separator inspection of rechargeable battery cells, where accurate geometric correction of CT is important to obtain high-resolution 3D CT images. In particular, this method can be applied in the medical field to the geometric information correction of the C-arm CT system, which is expected to be widely used in orthopedics and cerebrovascular surgery in the future. However, geometric wobbling occurs frequently due to the unstable gantry structure. In general, this method can be used for X-ray equipment that requires periodic quality assurance for geometric correction. In addition, if the movement of the object can be converted into the movement of the X-ray source and the detector, the proposed method can be applied to a patient's motion correction.

5 | CONCLUSION

In this study, we developed a PDGCM to compensate for motion-induced artifacts due to scanning device vibration during scanning in a rotating CL system. The method corrected mechanical errors without using a dedicated geometric correction phantom, and through simulated and experimental data, we confirmed that it was effective at performing geometric corrections. By avoiding the requirement for a dedicated phantom, we anticipate that this PDGCM will simplify the geometric correction process. In addition, by applying the process to high-magnification CL scan images, we confirmed that it had good accuracy and robustness. In future research, we plan to combine artificial intelligence methods to improve geometric correction performance of the PDGCM at high magnifications of 100× or above.

ACKNOWLEDGMENTS

The authors would like to thank SEC Co., Ltd. for providing the valuable CL scan images of the PCB. This work was supported by the Korea Medical Device Development Fund grant funded by the Korea government (the Ministry of Science and ICT, the Ministry of Trade, Industry and Energy, the Ministry of Health & Welfare, the Ministry of Food and Drug Safety) (Project Number: KMDF_PR_20200901_0016, 9991006689).

CONFLICT OF INTEREST

The authors declare that there are no conflicts of interest.

ORCID

Seung-Hoon Chae  <https://orcid.org/0000-0002-4115-1345>

Kihong Son  <https://orcid.org/0000-0003-4105-9028>

Sooyeul Lee  <https://orcid.org/0000-0002-7902-0690>

REFERENCES

- N. S. O'Brien, R. P. Boardman, I. Sinclair, and T. Blumensath, *Recent advances in X-ray cone-beam computed laminography*, *J. Xray Sci. Technol.* **24** (2016), no. 5, 691–707.
- P. Aryan, S. Sampath, and H. Sohn, *An overview of non-destructive testing methods for integrated circuit packaging inspection*, *Sensors* **18** (2018), no. 7, 1981. <https://doi.org/10.3390/s18071981>
- S. L. Fisher, D. J. Holmes, J. S. Jørgensen, P. Gajjar, J. Behnsen, W. R. B. Lionheart, and P. J. Withers, *Laminography in the lab: Imaging planar objects using a conventional x-ray CT scanner*, *Meas. Sci. Technol.* **30** (2019), no. 3, 35401.
- L. De Chiffre, S. Carmignato, J. P. Kruth, R. Schmitt, and A. Weckenmann, *Industrial applications of computed tomography*, *CIRP Ann.* **63** (2014), no. 2, 655–677.
- N. O'Brien, M. Mavrogordato, R. Boardman, I. Sinclair, S. Hawker, and T. Blumensath, *Comparing cone beam laminographic system trajectories for composite NDT*, *Case Stud. Nondestruct. Test. Evaluation.* **6** (2016), no. Part B, 56–61.
- H. Deyhle, H. Towsyfyfan, A. Biguri, M. Mavrogordato, R. Boardman, and T. Blumensath, *Spatial resolution of a laboratory based X-ray cone-beam laminography scanning system for various trajectories*, *NDT E Int.* **111** (2020). <https://doi.org/10.1016/j.ndteint.2020.102222>
- W. E. I. Long, *An industrial computed laminography imaging system*, (Proc. Digital Industrial Radiology and Computed Tomography, Belgium, Ghent), 2015, pp. 22–25.
- X. Pan, E. Y. Sidky, and M. Vannier, *Why do commercial CT scanners still employ traditional, filtered back-projection for image reconstruction?* *Inverse Probl.* **25** (2009), no. 12, 1230009.
- L. Yenumula, U. Kumar, and A. Dash, *X-ray industrial computed laminography (ICL) simulation study of planar objects: optimization of laminographic angle*, (Proc. Indian National Seminar & Exhibition on Nondestructive Evaluation NDE, Hyderabad, India), 2015.
- L. A. Feldkamp, L. C. Davis, and J. W. Kress, *Practical cone-beam algorithm*, *J. Opt. Soc. Am. A* **1** (1984), no. 6, 612–619.
- J. M. Que, D. Q. Cao, W. Zhao, X. Tang, C. L. Sun, Y. F. Wang, C. F. Wei, R. J. Shi, L. Wei, Z. Q. Yu, and Y. L. Yan, *Computed laminography and reconstruction algorithm*, *Chin. Phys. C.* **36** (2012), no. 8, 777.
- M. Yang, J. Zhu, Q. Liu, S. Duan, L. Liang, X. Li, W. Liu, and F. Meng, *A practical method to calibrate the slant angle of central X-ray for laminography scanning system*, *NDT E Int.* **64** (2014), 13–20.
- M. Yang, Z. Li, L. Liang, X. Li, W. Liu, and Z. Gui, *Automatic measurement of rotation center for laminography scanning system without dedicated phantoms*, *J. Electron. Imaging.* **23** (2014), no. 5, 53018.
- M. J. Daly, J. H. Siewerdsen, Y. B. Cho, D. A. Jaffray, and J. C. Irish, *Geometric calibration of a mobile C-arm for intraoperative cone-beam CT*, *Med. Phys.* **35** (2008), no. 5, 2124–2136.
- N. Navab, A. Bani-Hashemi, M. S. Nadar, K. Wiesent, P. Durlak, T. Brunner, K. Barth, and R. Graumann, *3D reconstruction from projection matrices in a C-arm based 3D-angiography system*, (Proc. International Conference on Medical Image Computing and Computer-Assisted Intervention, Cambridge, MA, USA), 1998, pp. 119–129.
- K. Wiesent, K. Barth, N. Navab, P. Durlak, T. Brunner, O. Schuetz, and W. Seissler, *Enhanced 3-D-reconstruction algorithm for C-arm systems suitable for interventional procedures*, *IEEE Trans. Med. Imaging* **19** (2000), no. 5, 391–403.
- R. R. Galigekere, K. Wiesent, and D. W. Holdsworth, *Cone-beam reprojection using projection-matrices*, *IEEE Trans. Med. Imaging* **22** (2003), no. 10, 1202–1214.
- F. Maes, D. Vandermeulen, and P. Suetens, *Medical image registration using mutual information*, *Proc. IEEE* **91** (2003), no. 10, 1699–1722.
- S. T. Kim, D. H. Kim, and Y. M. Ro, *Generation of conspicuity-improved synthetic image from digital breast tomosynthesis*, (Proc. 19th International Conference on Digital Signal Processing, Hong Kong, China), 2014, pp. 395–399.
- Z. Wang, A. C. Bovik, H. R. Sheikh, and E. P. Simoncelli, *Image quality assessment: From error visibility to structural*

- similarity, *IEEE Trans. Image Process.* **13** (2004), no. 4, 600–612.
21. M. Yang, J. Zhang, M. Yuan, X. Li, W. Liu, F. Meng, S. J. Song, and D. Wei, *Calibration method of projection coordinate system for X-ray cone-beam laminography scanning system*, *NDT E Int.* **52** (2012), 16–22.
 22. K. Yang, A. L. C. Kwan, D. W. F. Miller, and J. M. Boone, *A geometric calibration method for cone beam CT systems*, *Med. Phys.* **33** (2006), no. 6–1, 1695–1706.
 23. B. G. Chae and S. Lee, *Sparse-view CT image recovery using two-step iterative shrinkage-thresholding algorithm*, *ETRI J.* **37** (2015), no. 6, 1251–1258.
 24. M. J. Willemink and P. B. Noël, *The evolution of image reconstruction for CT-from filtered back projection to artificial intelligence*, *Eur. Radiol.* **29** (2019), no. 5, 2185–2195.

AUTHOR BIOGRAPHIES



Seung-Hoon Chae received his BS degree in electrical engineering and MS and PhD degrees in information and communication engineering from Chosun University, Gwangju, Republic of Korea, in 2007, 2009, and 2013, respectively. He is currently a senior researcher in ETRI, Daejeon, Republic of Korea. His current research interests include medical image processing, biometrics, and machine learning.



Kihong Son received his BS degree in radiological science from Yonsei University, Wonju, Republic of Korea, in 2009; MS degree in radiological cancer medicine from University of Science and Technology

(KIRAMS Campus), Daejeon, Republic of Korea, in 2012; and PhD degree in nuclear and quantum engineering from Korea Advanced Institute of Science and Technology, Daejeon, Republic of Korea, in 2017. He conducted visiting research at The University of Chicago, USA, from 2013 to 2014. He worked as a senior engineer for Samsung Electronics, Suwon, Republic of Korea, from 2017 to 2020. Since 2020, he has been working as a senior researcher in ETRI, Daejeon, Republic of Korea. His research interests include advanced medical image processing and reconstruction.



Sooyeul Lee received his BS, MS, and PhD degrees in physics from Seoul National University, Republic of Korea, in 1990, 1992, and 1997, respectively. Since 1998, he has been with ETRI. He is the leader of medical information research section of ETRI. His main research interests include medical imaging and medical image processing.

How to cite this article: S.-H. Chae, K. Son, and S. Lee, *Geometric calibration of a computed laminography system for high-magnification nondestructive test imaging*, *ETRI Journal* (2022), 1–10. <https://doi.org/10.4218/etrij.2021-0136>